

Cite this: *RSC Adv.*, 2014, 4, 31385

Solid-state phase transformation mechanism from hexagonal $\text{GdPO}_4 : \text{Eu}^{3+}$ nanorods to monoclinic nanoparticles†

Junsang Cho* and Chang Hae Kim

$\text{GdPO}_4 : \text{Eu}^{3+}$ nanorods with the hexagonal phase, prepared by a simple co-precipitation method at 80 °C, were transformed to $\text{GdPO}_4 : \text{Eu}^{3+}$ nanoparticles with the monoclinic phase upon heating above 800 °C. Based on the *in situ* observations of XRD, TEM, and SAED, we suggested the phase transformation mechanism of the hexagonal nanorods to monoclinic nanoparticles *via* diffusion-controlled solid-state transformation. This is associated with the formation of a void inside the nanorods because of the elimination of water, rearrangement of atomic structure, and nucleation and growth of nanoparticles with different crystal structure. Ultimately, prepared $\text{GdPO}_4 : \text{Eu}^{3+}$ nanorods and nanoparticles can be utilized as an efficient multifunctional nanoprobe for magnetic resonance (MR)/optical imaging due to the prominent orange-red emission of Eu^{3+} ions at 592 and 615 nm, and the exhibition of saturated magnetization value (M_s) of 0.52 emu $\text{g}^{-1} \text{Oe}^{-1}$ and high r_2/r_1 value.

Received 10th April 2014
Accepted 23rd June 2014

DOI: 10.1039/c4ra03229b

www.rsc.org/advances

Introduction

Recently, Gd^{3+} -based inorganic nanocrystals have attracted considerable interest because they can be used for magnetic resonance (MR)/optical imaging contrast agents in biomedical applications.^{1–3} The paramagnetic characteristic of Gd^{3+} ions because of the presence of several unpaired electrons in 4f shell allows their application as MR imaging contrast agents. At the same time, by incorporating light-emitting lanthanide ions into the host matrix, an effective multifunctional nanomaterial with fluorescent and magnetic properties can be easily fabricated within a single carrier.⁴ In fact, MR imaging offers excellent anatomical details in noninvasive and real time monitoring, and optical imaging provides high resolution.⁵ Thus, Gd^{3+} -based inorganic nanocrystals can serve as promising alternatives to conventional luminescent labels such as dye molecules and quantum dots (QDs) because of advantageous luminescence features, including high quantum yield, large Stokes shift, abundant energy level transitions, narrow emission band width, long fluorescent life time, low toxicity and high photochemical stabilities.^{6–9}

Among several Gd^{3+} ions-containing host systems, gadolinium phosphate (GdPO_4) has been well investigated because of its desirable biocompatibilities, resulting from the existence of phosphate groups on the surface of nanocrystals.¹⁰ Therefore,

numerous chemical methods have been reported for the synthesis of lanthanide ion (Ln^{3+})-doped GdPO_4 nanocrystals such as hydrothermal reactions and several solution-based precipitation methods.^{5,11–14} Especially, Eu^{3+} -doped GdPO_4 nanocrystals are the most promising multifunctional system for multimodal biomedical imaging because of the superior optical features of Eu^{3+} ion compared to other lanthanide ions. Hence, they have been extensively studied for various sizes, morphologies, and their correlated multifunctional properties.^{13–16}

In fact, it has been known that GdPO_4 has allotropic forms in which two or more different crystal structure exist, depending on the preparation conditions (acidity, solvent, and annealing temperature): hexagonal, tetragonal, and monoclinic.^{17–19} Recently, the phase transformation of hexagonal GdPO_4 nanorods to monoclinic GdPO_4 nanoparticles attracted considerable attention because the optical properties of $\text{GdPO}_4 : \text{Eu}^{3+}$ are strongly correlated with the symmetry around Eu^{3+} and crystal structure.^{20,21} Luwang *et al.* reported that the hexagonal YPO_4 hydrated nanorods were prepared *via* a hydrothermal method, and transformed to tetragonal YPO_4 dehydrated nanoparticles upon heating at 800–900 °C.²⁰ It was revealed that the evaporation of water and formation of void inside the nanorods were closely related with the distortion of lattice and phase transformation. More recently, Sahu *et al.* also demonstrated that the $\text{GdPO}_4 : \text{Eu}^{3+}$ system, prepared in H_2O and EG medium, has a different crystal structure such as hexagonal and monoclinic because of the different solvents and the availability of the incorporation of water into different crystal structure. Accordingly, phase transformation only occurred in the sample prepared in aqueous media because crystal water in the hexagonal structure played a significant role in phase

Thin Film Materials Research Group, Korea Research Institute of Chemical Technology (KRIT), 141, Gajeong-ro, Yuseong, Daejeon 305-600, Korea. E-mail: jscho@krit.re.kr; Fax: +82-42-861-4151; Tel: +82-42-860-7227

† Electronic supplementary information (ESI) available: See DOI: 10.1039/c4ra03229b

transformation.²¹ Even though previous studies have investigated the phase transformation of hexagonal nanorods to monoclinic nanoparticles, the precise phase transformation involving the changes in morphology is not clear. There is no clear explanation of how the lattice distortion appeared and why the correlated phase transformation occurred upon heating on the basis of the solid-state phase transformation mechanism, including nucleation and growth mechanism of nanoparticles in terms of thermodynamics.

Here, we suggest a new phase transformation mechanism *via* diffusion-controlled solid-state phase transformation for the understanding of the formation of monoclinic nanoparticles from hexagonal nanorods when $\text{GdPO}_4 : \text{Eu}^{3+}$ nanorods were transformed to $\text{GdPO}_4 : \text{Eu}^{3+}$ nanoparticles.^{17,22} The proposed mechanism is based on the *in situ* observations of X-ray diffraction (*in situ* XRD), transmission electron microscopy (*in situ* TEM), and corresponding selected area electron diffraction (SAED), which offer decisive clues for phase transformation by monitoring the *in situ* changes in crystallographic structure and morphology upon simultaneous heating up to $\sim 900^\circ\text{C}$. In addition, we can explain that the corresponding changes in multifunctional (optical and magnetic) properties are dependent on crystal structure. Eventually, we can develop and design multifunctional nanoprobes with high efficiency in luminescence and magnetic properties based on the understanding of phase transformation. $\text{GdPO}_4 : \text{Eu}^{3+}$ nanorods and nanoparticles with excellent luminescent features of strong red emission at 592 and 615 nm and magnetic properties can be potentially used as efficient multifunctional contrast agents.

Experimental section

Chemicals

All the chemicals were analytical grade and used without further purification. $\text{Gd}(\text{NO}_3)_3 \cdot 6\text{H}_2\text{O}$ (99.99%), Eu_2O_3 (99.99%) and $(\text{NH}_4)\text{H}_2\text{PO}_4$ (99%) were purchased from Sigma-Aldrich.

Synthesis of $\text{GdPO}_4 : \text{Eu}^{3+} \cdot \text{H}_2\text{O}$ nanorods and $\text{GdPO}_4 : \text{Eu}^{3+}$ nanoparticles

$\text{Gd}_{1-x}\text{PO}_4 : \text{Eu}_x^{3+} \cdot \text{H}_2\text{O}$ nanorods were prepared by a co-precipitation route. The molecular ratio of $\text{Gd} : \text{Eu} = 1 - x : x$ could be deliberately controlled by varying the stoichiometric amount of Gd/Eu . In the synthesis, a fixed ratio of $\text{Gd} : \text{Eu} = 0.95 : 0.05$ was used. Initially, 0.95 mmol of $\text{Gd}(\text{NO}_3)_3$ was dissolved in 25 mL of D.I water under vigorous stirring in a 100 mL round-bottom flask. Then, it was mixed with 0.05 mmol of Eu_2O_3 dissolved with 0.30 mmol of nitric acid (30% v/v). When dissolving Eu_2O_3 in nitric acid, excess acid was removed by evaporation with the addition of water. An excessive amount of 1.25 mmol of $(\text{NH}_4)\text{H}_2\text{PO}_4$ dissolved in 10 mL of D.I water was added to the mixed Gd/Eu ionic solution by dropwise addition at 80°C and reacted for 30 min. The suspension products were centrifuged at 4000 rpm for 10 minutes and washed with D.I water several times. The as-prepared powders were dried overnight at 80°C for further characterizations. For the synthesis of separate $\text{GdPO}_4 : \text{Eu}^{3+}$ nanoparticles, the as-prepared $\text{GdPO}_4 : \text{Eu}^{3+} \cdot \text{H}_2\text{O}$

nanorods were annealed at 900°C in air for 2 hours, according to a previously reported method.^{11,12}

Characterizations

The *in situ* high temperature X-ray powder diffraction (*in situ* XRD) was performed with a Rigaku Ultima IV diffractometer equipped with a graphite-monochromator. X-ray diffractometry in reflection geometry was measured in a 2θ range from 10 to 60° using $\text{Cu K}\alpha$ radiation ($\lambda = 1.5405 \text{ \AA}$). The as-prepared $\text{GdPO}_4 : \text{Eu}^{3+}$ nanorods were heated from room temperature up to 900°C at a rate of $10^\circ\text{C min}^{-1}$ for 5 minutes before measurement. The reference data were obtained from the International Centre for Diffraction Data (ICDD). The size and morphology of samples were observed by transmission electron microscope (TEM) with an FEI Tecnai G2-20 S-Twin at an accelerating voltage of 200 kV for the *ex situ* samples. The *in situ* high resolution transmission electron microscope (*in situ* HR-TEM) measurements and selected area electron diffraction (SAED) patterns were obtained by JEOL-3011 operating at 300 kV at an increasing rate of $\sim 80\text{--}100^\circ\text{C min}^{-1}$ from room temperature up to 870°C . Thermal gravimetric and differential thermal analysis (TG-DTA) were carried out using SDT Q600 V20.9 Build 20 to analyze thermal characteristics under air conditions at a rate of $10^\circ\text{C min}^{-1}$ in the temperature range of $20\text{--}900^\circ\text{C}$. Magnetic properties were measured by vibrating sample magnetometer (VSM) with Microsense Ev9, at 300 K, applied magnetic field in the range of -10 kOe to 10 kOe. To measure the luminescent properties, photoluminescence (PL) excitation and emission spectra were recorded by PSI Darsapro-5000 system equipped with 500 W Xenon lamp. The composition of products was analyzed by energy dispersive X-ray spectrometer (EDS) with Bruker, Quantax 200 equipped with Si Drift Detector.

MR imaging

MR imaging was measured with 4.7 T MR imaging instruments using Biospec; Bruker, Ettlingen, Germany. Various concentrations of Gd^{3+} ion ($0\text{--}16.0 \text{ mM}$) dispersed in 0.5% agarose gel were used for relaxation time (T_1 and T_2) measurements. The concentration of Gd^{3+} was determined by inductively coupled plasma atomic emission spectrometry (ICP-AES) by Thermo Scientific iCAP 6500 duo. T_1 measurement conditions were as follows: the value of repetition time per echo time (TR/TE) was 8000 ms/7.76 ms, the number of excitation (NEX) was 1, the obtained MR images had a matrix size of 128×128 , a field of view (FOV) of 50×60 , and a slice thickness of 2 mm. T_2 measurement conditions were as follows: the value of repetition time per echo time (TR/TE) was 10 000 ms/7.5 ms, and other conditions were the same with T_1 measurement conditions.

Results and discussion

Solid-state phase transformation *via* diffusion-controlled process from $\text{GdPO}_4 : \text{Eu}^{3+} \cdot \text{H}_2\text{O}$ nanorods to $\text{GdPO}_4 : \text{Eu}^{3+}$ nanoparticles

In a typical synthesis, $\text{GdPO}_4 : \text{Eu}^{3+} \cdot \text{H}_2\text{O}$ nanorods with the hexagonal phase are prepared by a simple co-precipitation

method and/or *via* a hydrothermal process at $\sim 100^\circ\text{C}$, and they can be transformed to $\text{GdPO}_4 : \text{Eu}^{3+}$ nanoparticles with the monoclinic phase through a post annealing process at a high temperature above 800°C .¹⁷ As suggested from the chemical formula between nanorods and nanoparticles, crystal water appeared to play a crucial role in not only the changes in crystal structure from hexagonal to monoclinic but also the changes in morphology from nanorods to nanoparticles.

We systematically investigated the crystallographic evolution from the hexagonal phase to the monoclinic phase, based on the *in situ* XRD with simultaneous heating of the as-prepared nanorods up to the a temperature of 900°C (Fig. 1). The as-prepared $\text{GdPO}_4 : \text{Eu}^{3+}$ nanorods were indexed to the hexagonal phase of $\text{GdPO}_4 \cdot \text{H}_2\text{O}$ with a space group, $P3_121$ (PDF#-00-039-0232), as shown in Fig. 1a. However, the hexagonal phase of an as-prepared sample was gradually transformed to the monoclinic phase with on increasing the temperature. The intensity of the (100) peak of the hexagonal structure measured at 800°C with a 2θ of 14.802° became relatively weak compared to the intensity of the same peak measured below 800°C , indicating that the phase transformation appeared to occurred around 800°C . In addition, the intensity of the (200) peak of the monoclinic phase with a 2θ of 27.651° was significantly increased at that temperature (Fig. 1d). The XRD patterns measured at 900°C were exactly consistent with the diffraction patterns of the monoclinic phase of GdPO_4 with a space group, $P2_1/n$ (PDF#-01-083-0657), as shown in Fig. 1e. It seemed appeared that hexagonal nanorods are oriented along with the (100) plane (*i.e.* *c*-axis), or the growth direction of nanorods is parallel to the *c*-axis because (200) peak is the most intense and (100) peak is prominent in the hexagonal structure. Therefore, it was suggested that the reduction in the length of nanorods along *c*-axis or the disintegration of nanorods resulted in a decrease in the intensity of the (100) peak of hexagonal structure upon heating. It eventually disappeared with the appearance of new XRD patterns of the monoclinic. The most intense

peak shift was clearly observed from the 2θ value of 29.9° originating from the (200) lattice plane of the hexagonal to 29.6° generated from the (120) plane of the monoclinic during phase transformation (Fig. S1, ESI†). A more detailed explanation of phase transformation will be discussed below.

From the XRD analysis, the dehydration of water molecules existing in the hexagonal nanorods was considered to be a determinative factor for inducing phase transformation. Thus, thermogravimetric analysis (TGA) and differential thermal analysis (DTA) measurements of hydrated $\text{GdPO}_4 : \text{Eu}^{3+}$ nanorods were made (Fig. 2). TGA results revealed that the total weight loss was 8.1% in the range of 20 – 900°C , which was slightly different than the theoretically calculated value of 6.7% due to the physically adhered water molecules on the surface of the sample in spite of the pre-heating treatment at 80°C overnight. It has been reported that three different types of water molecules can be present in zeolite compounds such as external water, loosely bound zeolitic water, and tightly bound zeolitic water, which can be differentiated by evaporated temperatures from DSC.^{23–25} The first weight loss of 2.6% was found up to 120°C with a broad endothermic peak in the range of 50 – 100°C in the DTA curve because of the evaporation of external water physically adhered on the sample. The physically adsorbed external water could be removed at a low temperature compared with zeolitically bound water. The second weight loss of 3.8% was observed in the range of 120 – 200°C , corresponding to a strong endothermic peak at 190°C because of the release of loosely bound zeolitic water. The final weight loss of 1.7% in the range of 200 – 900°C was associated with the dehydration of tightly bound zeolitic water. Importantly, the exothermic peak in the broad range of 800 – 850°C represented phase transformation because the sample underwent crystallization involving the formation of a different crystal structure with different heat capacity; thus, less energy is required to increase the temperature.²⁴ On the basis of the results of XRD and TG-DTA, it was evident that the phase transformation from hexagonal to monoclinic started occurring at a high temperature of $\sim 800^\circ\text{C}$.

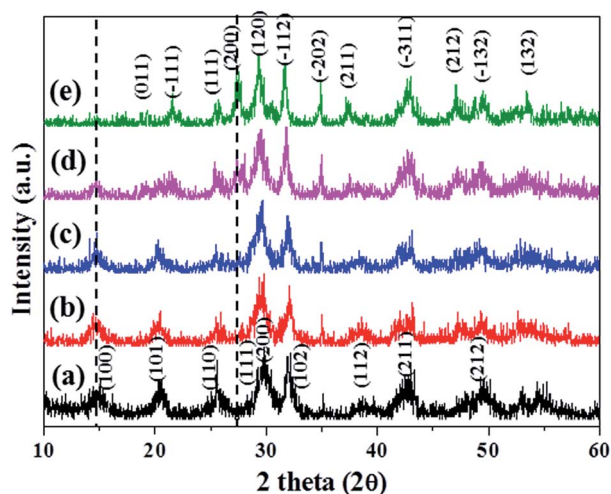


Fig. 1 *In situ* XRD measurement of $\text{GdPO}_4 : \text{Eu}^{3+}$ nanorods at different heating temperatures: (a) as-prepared, (b) 500°C , (c) 700°C , (d) 800°C , and (e) 900°C , respectively.

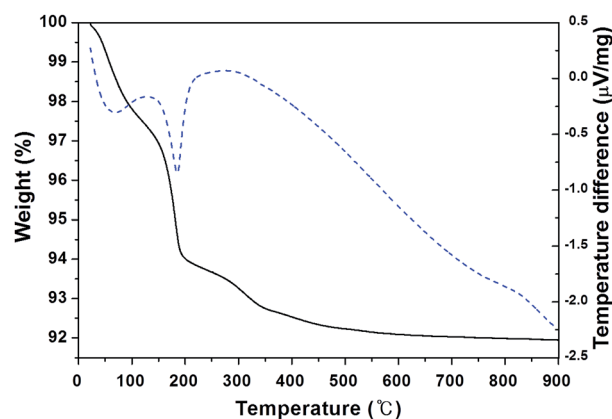


Fig. 2 Combined TG-DTA curves of the as-synthesized $\text{GdPO}_4 : \text{Eu}^{3+}$ nanorods: TGA (solid line) and DTA (dotted line).

The detailed *in situ* TEM images collected with SAED patterns were required to observe the *in situ* changes in crystal structure and morphology up on simultaneously heating the as-prepared sample up to 870 °C (temperature limit). The *in situ* TEM images revealed that nanorods maintained their rod-like shape until 500 °C but some voids appeared inside the nanorods (Fig. 3a). Upon further heating to 700 °C, an increased number of voids were produced because of the evaporation of water molecules along the *c*-axis of the hexagonal lattice (Fig. 3b).^{20,21} Upon further heating to 800 °C, lattice distortion was observed because of newly appearing nanoparticles with different lattice fringe and different crystal structure of the monoclinic against the present hexagonal nanorods. Eventually, nanorods appeared to be divided into several pieces of nanoparticles with a diameter of 5–10 nm at a higher temperature of 870 °C, indicated as round darker spots of crystallization, shown in Fig. 3d. More magnified TEM images made us to speculate that the formation of voids, lattice distortion, and appearance of darker spots is strongly associated with the deformation of nanorods and the formation of nanoparticles (Fig. S2, ESI†). The selected area electron diffraction (SAED) pattern collected along with the corresponding TEM images showed unambiguous changes in crystal structure. The as-prepared nanorods are well-matched with the diffraction patterns of the hexagonal structure, corresponding *hkl* plane indices of the hexagonal structure. At the intermediate structure where nanorods started transforming to nanoparticles around 700–800 °C, blurred diffraction patterns were observed, indicating that crystallinity of the hexagonal structure was destructed while new crystal structure of the monoclinic was constructed. When phase transformation was completed to some extent, diffraction patterns showed the monoclinic structure (Fig. S3, ESI†).

For a better understanding of the phase transformation mechanism in detail, the *in situ* HR-TEM measurements of one nanorod were obtained (Fig. 4a–e). It was noted that we tried to take HR-TEM measurements as quickly as possible to exclude the effect of an electron beam with high energy, probably causing the increase in the temperature of the as-prepared

nanorods and phase transformation in the end. Unfortunately, it was not possible to exclude it entirely because of the time required for focusing on the sample to obtain high resolution images. Nevertheless, it was significantly meaningful to note that solid nanorods were changed to the pore-generated nanorods on increasing the temperature. The schematic illustration of the phase transformation mechanism demonstrated that voids, pores and/or holes appeared inside nanorods, and nanoparticles formed around voids inside the nanorods upon heating up to 870 °C (Fig. 4f). It was suggested that the solid-state phase transformation of the hexagonal nanorods to the monoclinic nanoparticles occurred through diffusion-controlled solid-state reaction, including the heterogeneous nucleation of nanoparticles and their growth,^{22,26–28} according to the following steps: (1) formation of voids inside the nanorods, (2) nucleation of nanoparticles around the voids by an atomic rearrangement, and (3) simultaneous growth of nanoparticles *via* diffusion-controlled process with consuming nanorods; when nucleation occurred by an atomic redistribution, the most stable crystal structure of the monoclinic at high temperature above 800 °C appeared from the viewpoint of thermodynamics. In the solid-state phase transformation, diffusion-controlled and diffusion-less phase transformation occurred irrespective of the long range diffusion of atoms.^{26,27} In our case, there was incoming diffusion flux of atoms from the existing nanorods toward the newly formed nuclei of nanoparticles because it was shown that voids inside the nanorods became larger and the boundary of nanorods became vague upon heating, which were probably controlled by this diffusion-dependent solid-state reaction (Fig. 4b–d).

The solid-state phase transformation from the hexagonal nanorods to the monoclinic nanoparticles can be explained in terms of thermodynamics: (1) most stable crystal structure at a different temperature,^{17,24} (2) dehydration of water present in the hexagonal structure,²⁹ (3) increased surface energy because of the formation of voids inside the nanorods,^{30,31} and (4) decreased volume free energy because of the emergence of nanoparticles.^{26,27} In general, GdPO₄ is a well-known allotrope that can be crystallized in the tetragonal, hexagonal, and monoclinic structure.¹⁸ In this case, allotropic transformation can occur, depending on the annealing temperature. The

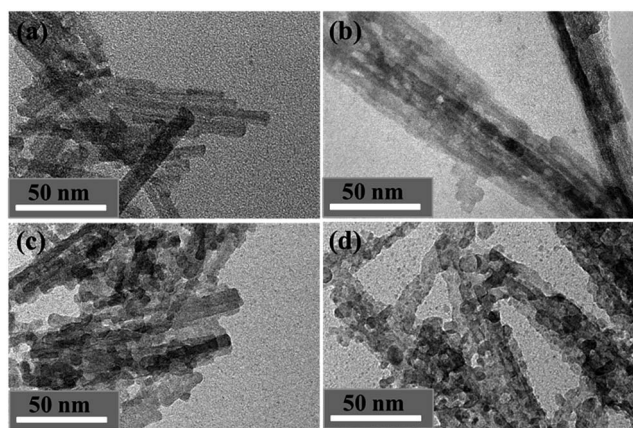


Fig. 3 *In situ* TEM measurements with heating GdPO₄ : Eu³⁺ nanorods at different temperatures: (a) 500 °C, (b) 700 °C, (c) 800 °C, and (d) 870 °C, respectively.

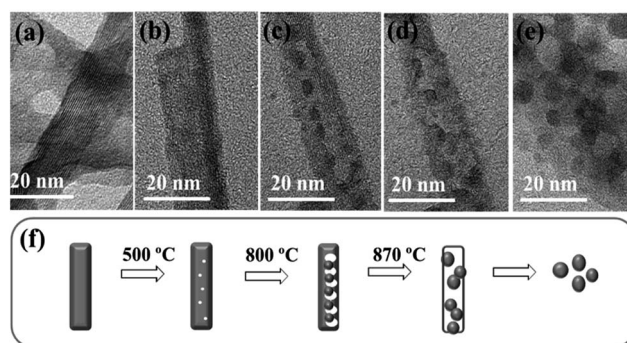


Fig. 4 *In situ* TEM measurements of a nanorod measured at (a) room-temperature, (b) 500 °C, (c) 800 °C, (d) 870 °C, (e) 870 °C (different spot) and (f) schematic illustration of the phase transformation mechanism *via* diffusion-controlled solid-state reaction.

hexagonal phase of GdPO_4 appeared to be the most stable structure at a low temperature in aqueous media because of the hexagonal stabilization energy of water because water molecules can be present on the pore along the c -axis such as a channel in hexagonal lattice.^{17,29} Therefore, GdPO_4 crystallized in the hexagonal nanorods with an anisotropic growth, directing toward c -axis, attributed to the intrinsic characteristic of building blocks and the chemical potential of specific lattice planes. Accordingly, Gd^{3+} cation and PO_4^{3-} anion were placed alternately on the hexagonal structure along [001] direction (c -axis) due to electrostatic Coulombic interaction. The activation energy for the growth to c -axis is lower than that of the growth perpendicular to the c -axis.¹⁷ Thus, it was suggested that the formation of the hexagonal system is kinetically driven at a relatively low reaction temperature, and the corresponding *Gibbs free energy* of the hexagonal structure (G_{hex}) is probably higher than that of the monoclinic (G_{mon}).

However, at an elevated temperature, the hexagonal structure could not be maintained because of the loss of water molecules, which are mandatory for the hexagonal structure. When water molecules were removed from the hexagonal structure, pore- and/or hole-generated nanorods appeared due to evaporation. The GdPO_4 molecules existing around pores probably had relatively higher surface energy compared with the same molecules in its solid counterpart because of highly increased surface area by the emergence of pores.³¹ Thus, to reduce the increased surface energy, atomic rearrangement occurred along with an emergence of voids. It was suggested that high temperature enabled atomic diffusion toward the surface of the voids, and nucleation preferably occurred around voids because with new phase it often appeared at certain sites within the metastable parent phase such as grain boundary, dislocation and defect sites in heterogeneous nucleation.²⁶ At certain monomer concentration of GdPO_4 adsorbed at the edge of voids, crystallization occurred for the nucleation of nanoparticles, which had the smallest surface energy because of the smallest surface-area-to-volume ratio. Moreover, it was evident that the nucleation of $\text{GdPO}_4 : \text{Eu}^{3+}$ nanoparticles prefer to be thermodynamically more stable in the monoclinic structure than the hexagonal because of sufficient freedom and energy to overcome activation energy for phase transformation when the bulk counterparts crystallized in the monoclinic phase at the temperature of 900–1000 °C.¹⁷ During nucleation and following the growth of nanoparticles, they were controlled by the interplay between volume energy (*Gibbs free energy*) and surface free energy (*interfacial energy*). When the spherical nuclei of nanoparticles are formed, they are stabilized by the change in volume energy while they are counter balanced by the introduction of surface energy of different crystal interface between the monoclinic and the hexagonal. In addition, the growth is strongly controlled *via* the diffusion-controlled process.^{26,27}

Corresponding multifunctional changes in optical/magnetic features along with phase transformation

In order to measure the changes in optical and magnetic features when during the phase transformation occurred, we

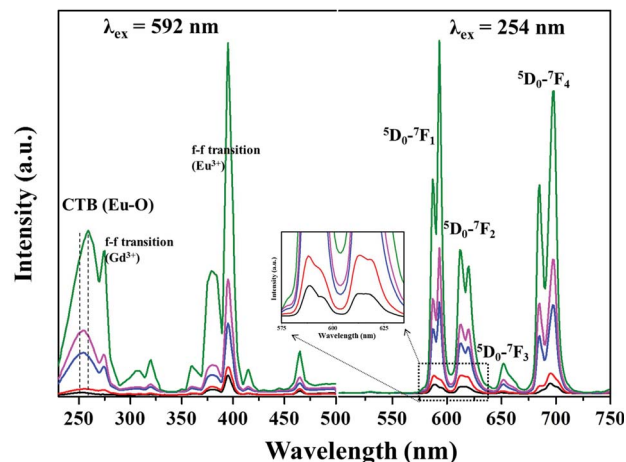


Fig. 5 PL excitation spectra recording the emission of 592 nm and emission spectra under the excitation of 254 nm of $\text{GdPO}_4 : \text{Eu}^{3+}$ samples annealed at various temperatures for 2 hours, respectively: from bottom to top, as-prepared, 500 °C, 700 °C, 800 °C, and 900 °C, respectively; inset shows the magnified PL emission in the range of 575–630 nm.

separately annealed the as-prepared samples at different temperatures, separately, from room-temperature (as-prepared) up to 900 °C. The crystal structure and morphology of the samples annealed at various temperatures was approximately coincident with the *in situ* results of TEM and XRD, as shown in Fig. S4, (ESI†). This was because there was no available the equipment of PL and MR imaging were not available for enabling measurements with simultaneous heating.

The room-temperature PL excitation and emission spectra of $\text{GdPO}_4 : \text{Eu}^{3+}$ nanocrystals annealed at various temperatures were recorded shown in Fig. 5. The excitation spectra were measured by monitoring the emission wavelength of 592 nm, which consisted of three parts: (1) broad band with a maximum of 240–260 nm due to the excitation of the charge transfer band (CTB) of $\text{Eu}^{3+}-\text{O}^{2-}$, (2) sharp peak at 275 nm due to the $4f^7$ to $4f^7$ transition of Gd^{3+} ($^8\text{S}_{7/2}-^6\text{I}_J$), and (3) several sharp lines in the range of 300–500 nm due to the excitation of Eu^{3+} ions transition from $4f^6$ to $4f^6$. Generally in general, CTB is a good indicator to offer the symmetry information of Eu^{3+} because CTB is strongly dependent on the coordination environment of Eu^{3+} and the corresponding length of the Eu–O bond.^{17,20} With annealing, CTB red-shifted to 10 nm for the sample annealed at 900 °C compared to the as-prepared sample. During phase transformation from the hexagonal to the monoclinic, the increase in coordination number (CN) from 8 to 9 resulted in lengthening the distance of Eu–O bond because of the expansion of Eu^{3+} cation into more available space in the monoclinic structure.^{17,32} It led to the red-shift of 10 nm of CTB. In addition, on annealing the as-prepared $\text{GdPO}_4 : \text{Eu}^{3+}$ at 800 °C, overall absorption intensity was increased because of the removal of water molecules, which played a key role in phonon-assisted quenching process (multi-phonon relaxation).^{20,33} The increase in excitation intensity for the sample annealed at 900 °C was associated with size effect. In fact, the particles with larger size had an improved crystallinity and decreased defect sites,

resulting in better excitation spectra. The emission spectra under a excitation wavelength of 254 show a magnetic dipole transition ($^5D_0-^7F_1$) at 592 nm, electric dipole transition ($^5D_0-^7F_2$) at 615 nm and ($^5D_0-^7F_4$) at 697 nm, and weak lines from the transition ($^5D_0-^7F_3$). The emission intensity was also increased significantly with annealing $GdPO_4 : Eu^{3+}$ samples at high temperature. The relative intensity ratio of the electric dipole transition ($^5D_0-^7F_2$) to the magnetic dipole transition ($^5D_0-^7F_1$), called the asymmetric ratio (I_{AS}), is an important parameter for understanding the symmetry around the Eu^{3+} in the crystal lattice, as shown in Fig. S5 and Table 1, ESI.† The electric dipole transition of $^5D_0-^7F_2$ highly sensitive to local symmetry indicated the asymmetric site occupied by Eu^{3+} ions, while the magnetic dipole transition of $^5D_0-^7F_1$ insensitive to the symmetry environment represented the symmetric site of Eu^{3+} ions. The value of I_{AS} for the as-prepared sample was close to 1. However, the value of I_{AS} became 1.24 for the sample annealed at 500 °C, and the ($^5D_0-^7F_2$) transition was dominant over the ($^5D_0-^7F_1$) transition, indicating that the environment around Eu^{3+} ions appears more asymmetric. Thus, it was suggested that more Eu^{3+} ions were located in the asymmetric site because of the evaporation of water and lattice distortion.^{34,35} On increasing the annealing temperature up to 900 °C, ($^5D_0-^7F_1$) transition increased compared to ($^5D_0-^7F_2$) transition and the value of I_{AS} decreased, indicating highly symmetric environments of Eu^{3+} ions with more available inversion sites. The intensities of emission spectra drastically increased because of the elimination of water molecules associated with the phonon-assisted quenching, as mentioned earlier. The emission peak position remained the same because of f-f transitions of Eu^{3+} ions which were not significantly affected by the outer crystal field.

The magnetic field-dependent magnetizations plots ($M - H$) of $GdPO_4 : Eu^{3+}$ nanorods and $GdPO_4 : Eu^{3+}$ nanoparticles were measured at 300 K, displayed in Fig. S6, ESI.† It was shown that the magnetization value of both nanorods and nanoparticles was similar. The saturated magnetization value of both samples measured at 10 kOe was found to be 0.52 emu g⁻¹ Oe⁻¹ and relevant mass magnetic susceptibility was 5.2×10^{-5} emu g⁻¹ Oe⁻¹. Due to the diamagnetism of water molecules, they had a little effect on the magnetization value because the diamagnetic contribution from water was negligible and paramagnetic contributions from the Gd^{3+} ions were dominant. With increasing the applied magnetic field strength, the magnetization value of both samples was linearly increased. Both 5 mol% Eu^{3+} -doped $GdPO_4$ nanorods and nanoparticles had the paramagnetic natures attributed from the same ratio of Gd^{3+} and Eu^{3+} ions due to unpaired electrons in 4f shells and energy dispersive X-ray spectrometer (EDS) analysis for the composition of them is shown in Fig. S7, ESI.†

The paramagnetic characteristics of $GdPO_4 : Eu^{3+}$ nanorods and nanoparticles were potentially applied to MR imaging contrast agents. The longitudinal relaxation rate (r_1 : $1/T_1$) and transverse relaxation rate (r_2 : $1/T_2$) were measured at various Gd^{3+} ion concentrations of both nanorods and nanoparticles dispersed in 0.5% agarose gel using the 4.7 T MR imaging instrument. The plots of reciprocal value of the longitudinal

relaxation rate (r_1) and transverse relaxation rate (r_2) against various Gd^{3+} ion concentrations are plotted in Fig. 6, respectively. For as-prepared $GdPO_4 : Eu^{3+}$ nanorods, a linear relationship was established between the relaxation rates (r_1 , r_2) and agent concentration (Fig. 6a and b). Relaxivity parameters were derived from the slope of the reciprocal values of the relaxation time ($1/T$) versus various Gd^{3+} ion concentrations and found to be $r_1 = 2.2$ and $r_2 = 57.5$ (s mM)⁻¹, respectively. With increasing the agent concentration, T_2 -weighted MR imaging showed negative contrast shown in Fig. 6e, which is consistent with previous results reported by Dumont *et al.* that undoped $GdPO_4 \cdot H_2O$ nanorods modified by phosphate ion on surface of the particles were effective contrast agents for T_2 -weighted MR imaging.¹⁰ Thus, as-prepared Eu^{3+} -doped nanorods can be classified as T_2 negative contrast agent because of high r_2/r_1 ratio of 26.1 and generation of negative MR contrast. In the same manner, the specific relaxivity parameters were measured for $GdPO_4 : Eu^{3+}$ nanoparticles and determined to be $r_1 = 0.2$ and $r_2 = 88.1$ (s mM)⁻¹ (Fig. 6c and d). It was considered that the value of the large ratio of r_2/r_1 was exaggerated because the value of the longitudinal relaxation rate (r_1) was extremely small compared to r_2 . It showed that $GdPO_4 : Eu^{3+}$ nanoparticles were very insensitive to the surrounding water at low concentration so that r_1 value was able to be derived at relatively high concentration of Gd^{3+} ions between 1–4 mM. It strongly indicated that nanoparticles were not effective positive MR contrast agent but effective negative one (Fig. 6f). Recently, Debasu *et al.*

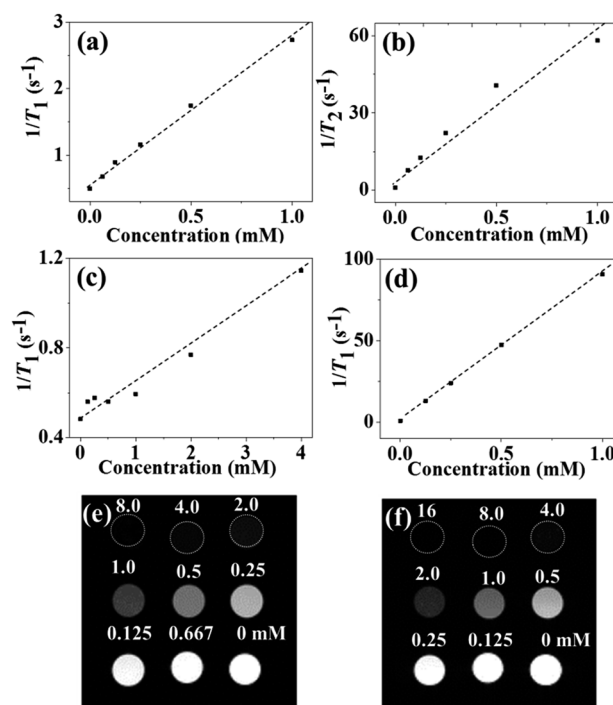


Fig. 6 Relaxivity parameters (r_1 , r_2) and T_2 -weighted MR images of $GdPO_4 : Eu^{3+}$ nanorods and nanoparticles: (a and b) plots of longitudinal (r_1) and transverse relaxation rate (r_2) of nanorods, (c and d) plots of longitudinal (r_1) and transverse relaxation rate (r_2) of nanoparticles, and (e and f) T_2 -weighted MR images of nanorods and nanoparticles, respectively.

also reported that Tb- and Yb-doped GdPO₄ nanoparticles annealed at 900 °C were proved to work as effective negative contrast agents.¹¹ This is because a high temperature treatment of the nanoparticles led to the non-availability of water molecules in crystal structure because of evaporation, and subsequently made them ineffective contrast for T_1 -weighted positive MR imaging.³⁶ Thus, in our case, the phase-transformed GdPO₄ : Eu³⁺ nanoparticles with monoclinic phase did not have inner water molecules in lattice structure so that they could not exchange with the bulk water efficiently. Consequently, nanoparticles could enhance the relaxivity through only outer-sphere relaxation mechanism while GdPO₄ : Eu³⁺ · H₂O nanorods could increase the relaxivity through both inner- and outer-sphere relaxation mechanism, indicating that nanorods had better r_1 value than that of nanoparticles. In fact, without the aid of hydrophilic polymer on the surface of the nanocrystals and MR measurements made at relatively weak magnetic field (<1.47 T) in order to increase the retention time of waters, it is very much challenging to develop GdPO₄ nanoparticles for positive T_1 -weighted MR imaging agents.¹¹ In our study, both nanocrystals can be used as potential T_2 -enhanced and/or negative MR imaging contrast agents due to the high r_2/r_1 ratio.

Conclusions

In this study, we demonstrated the diffusion-controlled solid-state phase transformation mechanism of the hexagonal GdPO₄ : Eu³⁺ nanorods to the monoclinic nanoparticles. The phase transformation involved several steps such as the formation of voids along with the evaporation of water molecules, rearrangement of surface atom toward voids, and the nucleation and growth of nanoparticles, which are controlled by solid-state diffusion-dependent process. This led to the formation of energetically more stable crystal structure of the monoclinic of GdPO₄ : Eu³⁺ nanoparticles at a high temperature of ~800 °C to reduce increased surface free energy, based on the *in situ* observation of XRD, TEM, and SAED. Ultimately, both GdPO₄ : Eu³⁺ nanorods and nanoparticles had red emission at 592 nm and 615 nm, saturated magnetization value of 0.52 emu g⁻¹ Oe⁻¹, and high r_2/r_1 ratio, enabling their application as multifunctional imaging, especially as T_2 -enhance contrast agent.

Acknowledgements

This work is financially supported by Korea Research Council for Industrial Science and Technology (ISTK) with the project number of KK-1307-B9. The author thanks for the measurement and analysis of the *in situ* TEM and corresponding SAED by Sung-In Kim at National Nanofab Center at Korean Advanced Institute of Science and Technology (KAIST).

Notes and references

- 1 J. Cheon and J.-H. Lee, *Acc. Chem. Res.*, 2008, **41**, 1630–1640.
- 2 A. Louie, *Chem. Rev.*, 2010, **110**, 3146–3195.

- 3 J. Kim, Y. Piao and T. Hyeon, *Chem. Soc. Rev.*, 2009, **38**, 372–390.
- 4 L. G. Jacobsohn, B. L. Bennett, R. E. Muenchausen, S. C. Tornga, J. D. Thompson, O. Ugurlu, D. W. Cooke and A. L. Lima Sharma, *J. Appl. Phys.*, 2008, **103**, 104303.
- 5 W. Ren, G. Tian, L. Zhou, W. Yin, L. Yan, S. Jin, Y. Zu, S. Li, Z. Gu and Y. Zhao, *Nanoscale*, 2012, **4**, 3754–3760.
- 6 J.-C. G. Bünzli, *Chem. Rev.*, 2010, **110**, 2729–2755.
- 7 S. Heer, O. Lehmann, M. Haase and H.-U. Güdel, *Angew. Chem., Int. Ed.*, 2003, **42**, 3179–3182.
- 8 K. Kömpe, H. Borchert, J. Storz, A. Lobo, S. Adam, T. Möller and M. Haase, *Angew. Chem., Int. Ed.*, 2003, **42**, 5513–5516.
- 9 F. Meiser, C. Cortez and F. Caruso, *Angew. Chem., Int. Ed.*, 2004, **43**, 5954–5957.
- 10 M. F. Dumont, C. Baligand, Y. Li, E. S. Knowles, M. W. Meisel, G. A. Walter and D. R. Talham, *Bioconjugate Chem.*, 2012, **23**, 951–957.
- 11 M. L. Debasu, D. Ananias, S. L. C. Pinho, C. F. G. C. Geraldies, L. D. Carlos and J. Rocha, *Nanoscale*, 2012, **4**, 5154–5162.
- 12 T. Grzyb, A. Gruszczyńska, R. J. Wiglus, Z. Sniadecki, B. Idzikowski and S. Lis, *J. Mater. Chem.*, 2012, **22**, 22989–22997.
- 13 L. Zhang, M. Yin, H. You, M. Yang, Y. Song and Y. Huang, *Inorg. Chem.*, 2011, **50**, 10608–10613.
- 14 Z. Xu, Y. Cao, C. Li, P. a. Ma, X. Zhai, S. Huang, X. Kang, M. Shang, D. Yang, Y. Dai and J. Lin, *J. Mater. Chem.*, 2011, **21**, 3686–3694.
- 15 L. Yu, D. Li, M. Yue, J. Yao and S. Lu, *Chem. Phys.*, 2006, **326**, 478–482.
- 16 S. Lu, J. Zhang, J. Zhang, H. Zhao, Y. Luo and X. Ren, *Nanotechnology*, 2010, **21**, 365709.
- 17 Y.-P. Fang, A.-W. Xu, R.-Q. Song, H.-X. Zhang, L.-P. You, J. C. Yu and H.-Q. Liu, *J. Am. Chem. Soc.*, 2003, **125**, 16025–16034.
- 18 Y. W. Zhang, Z. G. Yan, L. P. You, R. Si and C. H. Yan, *Eur. J. Inorg. Chem.*, 2003, **2003**, 4099–4104.
- 19 S. Rodriguez-Liviano, A. I. Becerro, D. Alcántara, V. Grazú, J. M. de la Fuente and M. Ocana, *Inorg. Chem.*, 2012, **52**, 647–654.
- 20 M. N. Luwang, R. Ningthoujam, S. Srivastava and R. Vatsa, *J. Am. Chem. Soc.*, 2011, **133**, 2998–3004.
- 21 N. K. Sahu, R. Ningthoujam and D. Bahadur, *J. Appl. Phys.*, 2012, **112**, 014306–014312.
- 22 Z. A. Peng and X. Peng, *J. Am. Chem. Soc.*, 2002, **124**, 3343–3353.
- 23 G. D. Knowlton and T. R. White, *Clays Clay Miner.*, 1981, **29**, 403–411.
- 24 R. Kijkowska, *Thermochim. Acta*, 2003, **404**, 81–88.
- 25 R. Kijkowska, E. Cholewka and B. Duszak, *J. Mater. Sci.*, 2003, **38**, 223–228.
- 26 C. Carter, *Kinetics of Materials*, Wiley-Interscience, 1st edn, 2005.
- 27 F. Liu, F. Sommer, C. Bos and E. Mittermeijer, *Int. Mater. Rev.*, 2007, **52**, 193–212.
- 28 M. Grünwald and C. Dellago, *J. Chem. Phys.*, 2009, **131**, 164116.
- 29 R. Mooney, *Acta Crystallogr.*, 1950, **3**, 337–340.

- 30 A. Navrotsky, *Geochem. Trans.*, 2003, **4**, 34–37.
- 31 S. Xiong, W. Qi, Y. Cheng, B. Huang, M. Wang and Y. Li, *Phys. Chem. Chem. Phys.*, 2011, **13**, 10648–10651.
- 32 R. Yan, X. Sun, X. Wang, Q. Peng and Y. Li, *Chem.–Eur. J.*, 2005, **11**, 2183–2195.
- 33 M. N. Luwang, R. Ningthoujam, S. Srivastava and R. Vatsa, *J. Am. Chem. Soc.*, 2010, **132**, 2759–2768.
- 34 N. Yaiphaba, R. Ningthoujam, N. Shanta Singh, R. Vatsa and N. Rajmuhon Singh, *J. Lumin.*, 2010, **130**, 174–180.
- 35 A. Parchur and R. Ningthoujam, *RSC Adv.*, 2012, **2**, 10859–10868.
- 36 G. A. Pereira, J. A. Peters, F. A. Almeida Paz, J. o. Rocha and C. F. G. C. Geraldies, *Inorg. Chem.*, 2010, **49**, 2969–2974.